Post-critical *SsPmp* and its Applications to Virtual Deep Seismic Sounding
2. 1D Imaging of the Crust/Mantle and Joint Constraints with Receiver Function

Tianze Liu[1] (tianze@stanford.edu), Simon L. Klemperer[1], Gabriel Ferragut[2,3], Chunquan Yu[4,5]
1. Department of Geophysics, Stanford University
2. Department of Geosciences, North Dakota State University
3. Department of Earth Sciences, University of Oregon
4. Seismological Laboratory, California Institute of Technology
5. Department of Earth and Space Sciences, Southern University of Science and Technology

Abstract

Virtual Deep Seismic Sounding (VDSS) has recently emerged as a novel method to image the crust-mantle-boundary (CMB) and potentially other lithospheric boundaries. In Liu et al., 2018 ("Part 1"), we showed that the arrival time and waveform of post-critical *SsPmp*, the post-critical reflection phase at the CMB used in VDSS, is sensitive to multiple attributes of the crust and upper mantle. Here, we present a synthesis on the methodology of deriving Moho depth, crustal average V_p and uppermost mantle V_p from single-station observations of post-critical *SsPmp* under an 1D assumption. We first verify our methods on synthetic examples and then substantiate it with a case study using data collected by the Yellowknife and POLARIS array in SW Slave Province, which shows good agreement between crustal and upper-mantle properties derived with VDSS and the ones given by previous studies using active source experiments and conventional P receiver functions (PRF). Moreover, we show that PRF-VDSS joint analysis is capable of placing tighter constraint on average crustal composition, which cannot be achieved with either method alone. We demonstrate with our PRF-VDSS joint analysis that the SW Slave Province, Canada has an intermediate crust composition, which likely indicates a Neoarchean age.

1. Introduction

In recent years, Virtual Deep Seismic Sounding (VDSS) has emerged as a novel method to image the crust-mantle boundary (CMB) and has been successfully applied to multiple datasets from different areas (e.g. Kang et al., 2016; Parker et al., 2016; Tseng et al., 2009; Yu et al., 2012, 2016). *SsPmp*, the seismic phase used in VDSS, originates when upcoming teleseismic S waves convert to down-going P waves at the free surface (the virtual source), which then undergo post-critical reflection at or within the CMB and finally reach the receiver (Fig. 1c).

(Here we use *CMB* to denote the boundary or geological transition from crust to mantle, whether abrupt or a "velocity-gradient zone" spanning many kilometers; and *Moho* to denote a seismological inference about this transition, typically given as a single depth.) The arrival time of *SsPmp* relative to the direct S arrival (or *Ss*), hereafter T_{VDSS}, is used to estimate the Moho depth at the reflection point, commonly assumed to be the midpoint between the virtual source and receiver. Because VDSS uses teleseismic events, the incident S wave is usually approximated as a plane wave with constant ray parameter. To enable post-critical reflection of *SsPmp* at the CMB, appropriate epicentral distances are ~30–50º (Yu et al., 2016), corresponding to ray parameter $p = $ ~0.1256–0.1409 s/km for a focal depth of 0 km ($1/p = $ ~7.10–7.96 km/s) (Liu et al., 2018), and slightly smaller p for larger focal depths. Due to post-critical reflection at the CMB, *SsPmp* usually has amplitude comparable to *Ss* (Fig. 1b), making it possible to construct a seismic profile with a single event recorded by an array. Because *SsPmp* undergoes post-critical reflection at the CMB, its phase is changed relative to *Ss* (e.g. Aki and Richards, 1980) (Fig. 1b; hereafter referred to as phase shift for simplicity and denoted Φ_{VDSS}), making it difficult to directly pick T_{VDSS} from raw records. Previous studies (e.g. Tian et al., 2015; Tseng et al., 2009; Yu et al., 2016) have used 1D waveform fitting to measure T_{VDSS}, and then found the trade-off relation between average crustal V_p^{av} and thickness H using the equation:

$$T_{VDSS} = 2H\sqrt{\frac{1}{V_p^{av\,2}} - p^2} \qquad (1)$$

where p is the ray parameter of *Ss* and *SsPmp*. In our previous paper (Liu et al., 2018), using 1D synthetic tests, we found that whereas T_{VDSS} is primarily determined by CMB depth and crustal average V_p, Φ_{VDSS} is sensitive to lower-crustal and uppermost-mantle V_p (V_p^{lc} and V_p^{um}), which implies the possibility of constraining V_p^{lc} and V_p^{um} with observations of Φ_{VDSS}.

Here, we first show that T_{VDSS} can be estimated by picking peaks on *SsPmp* envelope functions, which can be used to derive Moho depth. We then present synthetic tests to demonstrate that V_p^{um} can be constrained without a priori knowledge of V_p^{um} using post-critical *SsPmp* with turning velocity $1/p$ close to V_p^{um}. We finally present a case study using data collected by the Yellowknife and POLARIS array in the SW Slave Province, which shows good agreement between crustal and upper-mantle properties derived by us with VDSS and the ones from previous studies using active-source experiments and our own conventional P receiver functions (PRF). Specifically, our V_p^{um} agrees with *Pn* velocity derived with seismic refraction

experiments (Hammer et al., 2010), and our VDSS Moho depth matches the Moho depth given by both seismic reflection experiments (Hammer et al., 2010) and our PRF. In addition, we demonstrate that by joint analysis of PRF and VDSS, we can simultaneously estimate average crustal V_p and V_p/V_s ratio, thereby placing tight constraints on average crustal composition.

2. Synthetic Examples

2.1. Measuring T_{VDSS} from Envelope Functions

When a signal undergoes a phase shift, despite the change of its waveform, its envelope function stays constant (Aki and Richards, 1980a). Therefore, a simple way to account for the phase shift of *SsPmp* relative to *Ss* while measuring T_{VDSS} is to calculate the time between the peaks on *Ss* and *SsPmp* envelope functions (Parker et al., 2016). Fig. 2a shows synthetic waveforms calculated using the reflectivity algorithm (Randall, 1989) for the 1D models in Fig. 1 (hereafter "Model #1") and $0.124 \leq p \leq 0.140$ s/km, after separation into pseudo-P (motion associated with incoming S waves) and pseudo-S (motion associated with incoming P waves) components (hereafter referred to as P and S for simplicity) with a particle-motion analysis algorithm (Yu et al., 2013) and converting to envelope functions. The shapes of *Ss* (S component) and *SsPmp* (P component) envelope functions are essentially identical, as the arrivals are only distinguished by a phase shift (Φ_{VDSS}), a negligible amplitude change due to post-critical reflection, and a time delay. We then measure T_{VDSS} from these *Ss* and *SsPmp* envelope functions and convert them to Moho depths using Eq. 1 and the true average crustal V_p. The estimated Moho depths agree (within 0.1 km) with the true CMB depth for all p (Fig. 2b), indicating the robustness of this method. We note that given multiple *SsPmp* observations with a wide range of ray parameter p, as in our example here, we can simultaneously determine Moho depth and crustal average V_p (Kang et al., 2016), as shown below in our analysis of observations from the SW Slave Province (see Section 3). Although T_{VDSS} can be robustly estimated from *SsPmp* envelope functions, when calculating these envelope functions we effectively eliminate the information contained in Φ_{VDSS} (Fig. 2a), which is sensitive to the structure of the CMB (Liu et al., 2018). Therefore, a more desirable way to analyze *SsPmp* is to model T_{VDSS} and Φ_{VDSS} simultaneously.

2.2. Modeling T_{VDSS} and Φ_{VDSS} Simultaneously

In order to measure T_{VDSS} and Φ_{VDSS} simultaneously, we first generate synthetic $SsPmp$ waveforms for all combinations of V_p in the lower crust (V_p^{lc}) and upper mantle (V_p^{um}) using the reflection coefficient at the Moho (Aki and Richards, 1980b). We then use cross-correlation to align the synthetic $SsPmp$ waveforms with the "observed" data (e.g. the waveforms in Fig. 1b) and compute the normalized misfit (hereafter referred to as misfit for simplicity) between the synthetic and "observed" $SsPmp$. Before computing the misfit, we normalize the "observed" and synthetic $SsPmp$ by the peak values of their envelope functions so that the effects of amplitude difference are eliminated. The synthetic $SsPmp$ waveform with the minimum misfit determines the best-fit V_p^{lc} and V_p^{um}, and the best-fit T_{VDSS} is found by picking the peak cross-correlation value between the best-fit synthetic $SsPmp$ and the "observed" one. Note that previous 1D modeling schemes have held V_p^{lc} and/or V_p^{um} fixed (Tian et al., 2015; Tseng et al., 2009; Yu et al., 2016). To test this approach, we use the reflectivity method (Randall, 1989) to compute "observed" waveforms and try to recover T_{VDSS}, V_p^{lc} and V_p^{um} from them using the method described above.

We first attempt to recover both V_p^{lc} and V_p^{um} from the observed $SsPmp$ waveforms. Our "observed" waveforms are computed with Model #1, a single layer crust with $V_p = 6.5$ km/s overlaying a half space with $V_p = 8.1$ km/s that represents the upper mantle (Fig. 1a). We assume two different ray parameters $p = 0.128$ and 0.136 s/km to study the potential effects of ray parameter. After applying our proposed method, the resulting misfits are plotted as functions of V_p^{lc} and V_p^{um} (Fig. 3). In the case with $p = 0.128$ s/km ($1/p = 7.81$ km/s), we observe that the misfit depends strongly on V_p^{um} and weakly on V_p^{lc}, with the misfit contours having small negative slopes (negative trade-off between V_p^{lc} and V_p^{um}; Fig. 3). In contrast, in the case with $p = 0.136$ s/km ($1/p = 7.35$ km/s), although the trade-off between V_p^{lc} and V_p^{um} is still negative, the misfit depends weakly on both V_p^{lc} and V_p^{um} (Fig. 3b). [Note that because the observed and synthetic waveforms are not computed in the same way, minor differences exist between them that makes the minimum misfits in both cases non-zero (Fig. 3).] Because fitting $SsPmp$ waveforms is equivalent to fitting Φ_{VDSS}, this behavior of misfit can be understood by considering the dependence of Φ_{VDSS} on V_p^{lc} and V_p^{um}. When $1/p$ is close to V_p^{um}, e.g. the case with $p = 0.128$ s/km ($1/p = 7.81$ km/s; Fig 3a), Φ_{VDSS} is primarily controlled by V_p^{um} with only weak dependence on V_p^{lc} (Liu et al., 2018). When $1/p$ is close to neither V_p^{um} nor V_p^{lc}, e.g. the case with $p = 0.136$ s/km ($1/p = 7.35$ k/s; Fig 3b), Φ_{VDSS} depends weakly on both V_p^{um} and V_p^{lc}

(Liu et al., 2018). Ideally, when $1/p$ is close to V_p^{lc}, misfit will be primarily controlled by V_p^{lc} due to the strong dependence of Φ_{VDSS} on V_p^{lc}. However, in this case the large p may cause strong pre-critical reflections from intra-crustal interfaces that may interfere with $SsPmp$ and distort its waveform (e.g. Fig. 5 in Liu et al., 2018). Therefore, a more practical way to utilize Φ_{VDSS} observations is to infer V_p^{um} from Φ_{VDSS} while assuming a known V_p^{lc} in cases with $1/p$ close to V_p^{um}, because in such cases an incorrect V_p^{lc} would only have limited effect on estimated V_p^{um} (Fig. 3a).

Fig. 4 shows examples of this strategy of estimating Moho depth and V_p^{um} from $SsPmp$ waveforms while fixing V_p^{lc}. We use the correct crustal average $V_p = 6.5$ km/s in Eq. 1 to convert the measured T_{VDSS} to Moho depth. For $p = 0.128$ s/km, when the true $V_p^{lc} = 6.5$ km/s (V_p^{lc} and average crustal V_p are the same here because the crust is homogeneous) is assumed, we are able to recover both the CMB depth and V_p^{um} precisely (Fig. 4a). As a result of the precisely recovered V_p^{um} and V_p^{lc}, the synthetic $SsPmp$ matches the observation almost perfectly (Fig. 4b). For the same "observed" data ($p = 0.128$ s/km), when we vary V_p^{lc} from the true value to 6.2 and 6.8 km/s (~5% perturbation), only ~0.6% error is introduced to the estimated V_p^{um} ($< \pm 0.05$ km/s), and its effect on estimated Moho depth is negligible (Fig. 4c). The misfit curves for $V_p^{lc} = 6.2, 6.5$ and 6.8 km/s have very similar minima, indicating that the synthetics fit the "observed" data equally well for all three cases (Fig. 4d). Because Φ_{VDSS} is matched precisely in all three cases, the correct T_{VDSS} is found in each case and we are able to give the correct CMB depth despite errors in assumed V_p^{lc} (Fig. 4c). To further explore the effects of p on the trade-off between V_p^{lc} and V_p^{um}, we infer Moho depth and V_p^{um} from "observed" $SsPmp$ waveforms with $p = 0.136$ s/km, again assuming $V_p^{lc} = 6.2, 6.5, 6.8$ km/s. In this case, a ~5% perturbation in V_p^{lc} causes ~1-2% error in the estimated V_p^{um}, significantly larger than the case with $p = 0.128$ s/km, whereas the effect on estimated Moho depth is still negligible due to the precisely matched $SsPmp$ waveforms (Fig. 4e). We also observe that the troughs of the misfit curves are significantly wider for $p = 0.136$ s/km than for $p = 0.128$ s/km, indicating poorer constraints on V_p^{um} (Fig. 4f). The above results show that, in a 1D earth, matching Φ_{VDSS} alone is sufficient to estimate T_{VDSS} and CMB depth precisely, whereas to infer V_p^{um} from Φ_{VDSS} requires a priori knowledge of V_p^{lc}. If V_p^{lc} is poorly constrained in the study region, it is better to use $SsPmp$ waveforms with $1/p$ close to V_p^{um} so that an incorrect assumed V_p^{lc} causes less error in the estimated V_p^{um}. Even in cases with well-constrained V_p^{lc}, using $SsPmp$ waveforms with $1/p$ close

to $V_p{}^{um}$ is still preferred because the narrower troughs of the misfit curves in such cases would result in better constrained $V_p{}^{um}$ (smaller uncertainty).

3. Observations from the SW Slave Province

The Canadian Shield is one of the Earth's largest cratons in the world. Its longevity and stability imply a lithospheric structure closer to 1D than in tectonically active areas. The Yellowknife Array was deployed in SW Slave Province, a major component of the Canadian Shield (Fig. 5a,b), in 1962 and was upgraded to digital recording in 1989 (Bostock, 1998). The long deployment time and its location at the core of the Canadian Shield makes it an ideal place to test our proposed method for retrieving and analyzing both T_{VDSS} and Φ_{VDSS} under 1D assumption. In addition, the SNorCLE component of the Lithoprobe project has accumulated rich material on crustal structure of the study area (e.g. Cook, 2002; Fernández-Viejo et al., 2005; Hammer et al., 2010), providing an unprecedented chance for direct comparison between VDSS and active-source results.

Among all the archived stations of the Yellowknife Array available in the Data Management Center of the Incorporated Research Institutions for Seismology (IRIS), the station YKW3 has the longest archived broadband recording (1994-2014). In addition, Station EDZN of the temporary POLARIS array (Snyder and Bruneton, 2007) was located ~80 km NW of YKW3, within 30 km of Moho reflection points of *SsPmp* recorded at YKW3 (Fig. 5b), making it appropriate to compare PRF results at EDZN with VDSS results at YKW3, as conversion points of PRFs at Moho depth are typically < 20 km away from the station. For VDSS analysis at YKW3, we used 56 teleseismic events in the epicentral range 30–60º with the back-azimuth range of 290–310º. We choose this narrow back-azimuth range to avoid possible complications from lateral variation in lithospheric structure (the Moho reflection points of our selected events are all within 25 km of each other (Fig. 5b)), while still including plenty of events from the Kamchatka subduction zone with a wide range of ray parameters (Figs. 5a, b). We then remove the instrumental response, apply a bandpass Butterworth filter between 0.05–0.5 Hz, and separate the radial and vertical components of the data to P and S components using a particle-motion analysis algorithm (Yu et al., 2013). After separating the data into P and S components, we manually inspect the traces and their particle-motion diagrams to choose 19 events with

simple *Ss* waveform and significant P energy following the S arrival. We then compute the envelope functions of the P and S components of the 19 events and select the ones with the ratio between the maxima of P envelope function and S envelope function > 0.6, which further reduce the number of events to 10. The selected 10 events all have simple *Ss* waveforms and strong *SsPmp* following the *Ss* arrival (Fig. 5b). When sorted by their ray parameter, the 10 traces show a clear increase of T_{VDSS} (moveout) with decreasing ray parameter (Fig. 5c), which can be used to simultaneously constrain the crustal average V_p and crustal thickness (Kang et al., 2016). In order to measure T_{VDSS} and Φ_{VDSS} simultaneously, for each event we use a cosine-tapered 20-s window around the *Ss* waveform on the S component as the source wavelet of that event. We then apply phase shifts from 0–360º to the source wavelet to create synthetic *SsPmp* waveforms with all possible phase shifts. For each synthetic *SsPmp* wavelet, we used cross-correlation to find the best alignment between it and the observed *SsPmp*. We then normalize both the observed and synthetic *SsPmp* and compute the misfit between them. The Φ_{VDSS} of the event is determined as the phase shift that minimizes the misfit between the synthetic and modeled *SsPmp* (Fig. 5d). We estimate the uncertainty of T_{VDSS} and Φ_{VDSS} from curvature of the Φ_{VDSS}-misfit function around the best-fit Φ_{VDSS} (See Supplementary Text 1 and Fig. S1). Here we apply another round of data selection that excludes the events with minimum misfit > 0.4, because a large misfit implies that the *SsPmp* of the event cannot be well approximated as phase-shifted from the source time function, which violates our basic assumption. This finally reduces the number of events to 7. The T_{VDSS} of each event is then found by cross-correlation between the best-fit synthetic *SsPmp* and the observed *SsPmp*. For PRF analysis at EDZN, we requested teleseismic P wave data between 30-90º from Canadian Hazards Information Service and used the time-domain iterative deconvolution algorithm with a Gaussian bandwidth of 2.5 Hz to compute PRFs (Herrmann, 2013). We manually selected 73 high-quality RFs using the Funclab software package (Porritt and Miller, 2018), which are moveout-corrected to normal incidence for primary *Ps* conversions and stacked (Fig. 6a). We also perform conventional *H-k* stacking with the selected RFs using the average crustal V_p = 6.62 km/s (hereafter V_p^{av}) constrained with VDSS analysis and a phase weight ratio $w_{Ps}:w_{PpPms}:w_{PpSms}$ = 1:0.5:0.5 (Fig. 6c) (Zhu and Kanamori, 2000).

The arrival time of the Moho *Ps* in PRF can be expressed as:

$$T_{Pms} = H \left(\sqrt{\left(\frac{k}{V_p^{av}}\right)^2 - p^2} - \sqrt{\left(\frac{1}{V_p^{av}}\right)^2 - p^2} \right) \tag{2}$$

in which k is the crustal average V_p/V_s ratio. Using H and V_p^{av} derived from *SsPmp* observations, we can derive k (hereafter k_{joint}) from T_{Ps}. Unlike the conventional *H-k* stacking method that relies on the Moho multiples (*PpPms*, *PpSms* etc.), our proposed method uses only *Ps*, the most robust phase in PRF observations. To estimate the uncertainty of our k_{joint}, we draw 5000 random samples of V_p^{av} and H_{VDSS} from their joint distribution (Kang et al., 2016) and compute k_{joint} for each pair. We estimate the uncertainty of our k_{joint} from the variance of the 5000 randomly simulated k_{joint} (Fig. 6b,c). Since V_p^{av} and k_{joint} together place key constraints on crustal average composition (Christensen, 1996; Christensen and Mooney, 1995), we also compute the joint distribution of V_p^{av} and k_{joint} (Fig. 8).

Our observed T_{VDSS} clearly decreases with increasing ray parameter, with a typical uncertainty of ± 0.3s (Fig. 5e). We find the best-fit crustal V_p^{av} and Moho depth (H_{VDSS}) to be 6.62 ± 0.20 km/s and 37.7 ± 4.2 km respectively (Fig. 5e; Kang et al., 2016). Our Moho depth is in good agreement with previous active source reflection results (~37 km) (Hammer et al., 2010) and is slightly deeper than by within uncertainty of seismic refraction results (~31-33 km)(Fernández-Viejo et al., 2005; Hammer et al., 2010), whereas our crustal average V_p is slightly higher than the value given by active-source refraction studies (~6.4 km/s) (Fernández-Viejo et al., 2005; Hammer et al., 2010). When comparing our VDSS Moho depth (H_{VDSS}) with the *H-k* Moho depth (H_{Hk}), we find a close match between them ($H_{VDSS} = 37.7$ km vs. $H_{Hk} = 37.3$ km; Fig. 6c). The agreement between H_{VDSS} and H_{Hk} not only verifies this result, but also indicates that 6.62 km/s is likely a reliable estimation of crustal average V_p.

Our Φ_{VDSS} shows a clear decrease with increasing ray parameter, in agreement with our theoretical predictions (Liu et al., 2018). To find the best-fit V_p^{um}, we plot theoretical p-Φ_{VDSS} relations with different V_p^{um} values while assuming $V_p^{lc} = 6.8$ km/s, the value given by active-source refraction studies (Fig. 5f; Hammer et al., 2010), and compare them with the observed values. The comparison shows that the observations favor $V_p^{um} = 8.0$-8.1 km/s, which agrees reasonably well with *Pn* velocity of ~8.2 km/s reported by the refraction studies (Fig. 5f) (Fernández-Viejo et al., 2005; Hammer et al., 2010). To test the effects of V_p^{lc} on the estimated V_p^{um}, we compare the theoretical curves computed by assuming $V_p^{lc} = 6.6, 6.8, 7.0$ km/s (~3%

perturbation; Fig. 7). We observe that for V_p^{lc} = 6.5 and 6.8 km/s, the theoretical p-Φ_{VDSS} curves overlap when p is small and gradually diverge as p increases (Fig. 7), but never to the extent that may affect the estimated V_p^{um}, especially when the uncertainties of our observed Φ_{VDSS} (~20°) is considered (Fig. 7). The theoretical p-Φ_{VDSS} relations are insensitive to assumed V_p^{lc} because the reciprocal of ray parameter ($1/p$) considered here (7.5-8.1 km/s) is significantly higher than the assumed V_p^{lc}, which makes Φ_{VDSS} insensitive to V_p^{lc} (Liu et al., 2018). In the case of V_p^{lc} = 6.6 km/s (7.0 km/s), the theoretical p-Φ_{VDSS} curves are shifted slightly upward (downward) compared to the case with V_p^{lc} = 6.8 km/s, because for a fixed ray parameter, decreasing (increasing) V_p^{lc} while fixing Φ_{VDSS} requires an increase (decrease) in V_p^{um} (negative trade-off between V_p^{lc} and V_p^{um}; Liu et al., 2018).

We observe clear Moho Ps at 4.24 s and little energy from intra-crustal convertors on the normal-moveout-stacked PRF of EDZN (Fig. 6a), in contrast to clear interfaces between upper, middle and lower crust shown by active-source refraction results (Hammer et al., 2010). The PRFs plotted as a function of back-azimuth (Fig. S2) are uniform, further supporting our 1D assumption as they show no evidence of dip on the Moho or anisotropy in the crust. Using our T_{Ps}, V_p^{av} and H_{VDSS}, we find k_{joint} = 1.745±0.061 (Fig. 6b), which matches k_{Hk} very well (k_{joint} = 1.745 vs. k_{Hk} = 1.754). This agreement, together with the close match between H_{VDSS} and H_{Hk}, demonstrate the robustness of our method.

The joint distribution between V_p^{av} and k_{joint} shows a clear negative correlation between them (Fig. 8). We also plot V_p and k of major crustal rock types measured at 600 MPa (corresponds to mid-crustal depth) and room temperature from Christensen 1996, which shows a positive correlation between V_p and k (Fig. 8). We note that temperature effects on both rock V_p/V_s ratio and V_p are small compared to the uncertainties of each rock type (Christensen, 1996; Christensen and Mooney, 1995). As the SiO_2 content of the rock increases (more felsic), both the V_p/V_s ratio and V_p of it decreases (Fig. 8). Because our observed V_p-k correlation is opposite to the V_p-k correlation of laboratory measurements, we could tightly constrain the average crustal composition in our study area as diorite or felsic granulite (Fig. 8).

4. Discussion

Post-critical $SsPmp$ has 3 major attributes: T_{VDSS}, Φ_{VDSS} and A_{VDSS}. In 1D, A_{VDSS} is only affected by near-surface velocity (Liu et al., 2018), whereas T_{VDSS} and Φ_{VDSS} both contain

information on crustal and upper-mantle structure. In this paper, we propose methods to retrieve Moho depth, V_p^{av} and V_p^{um} from *SsPmp* observations under the 1D assumption.

Φ_{VDSS} is controlled by V_p^{lc} and V_p^{um} and can be measured from *SsPmp* by waveform fitting (Figs. 3 and 4). Due to the trade-off between V_p^{lc} and V_p^{um}, it is impossible to determine one without knowing the other (Fig. 3). However, we show that when p is small ($1/p$ close to V_p^{um}), Φ_{VDSS} depends only weakly on V_p^{lc}, allowing determination of V_p^{um} without a precisely known V_p^{lc} (Fig. 3 and 4; Liu et al., 2018). Although V_p^{um} can be derived from a single *SsPmp* observation (Fig. 4), a combination of Φ_{VDSS} from multiple *SsPmp* traces can significantly reduce estimation error (Fig. 5). We note that, when measuring Φ_{VDSS}, it is important to choose only traces with high signal-to-noise ratio, as waveform observables are more sensitive to noise than travel-time measurements. This is especially true when considering the higher noise level of teleseismic S compared to P wave due to coda waves generated by preceding P phases that arrive in the same time window. A practical criterion for data quality control is to choose *SsPmp* traces that can be well-fit with a phase-shifted *Ss* wavelet (Fig. 5). When comparing our derived V_p^{um} with the *Pn* velocity given by active-source refraction experiments (Fernández-Viejo et al., 2005; Hammer et al., 2010), we find our result to be slightly lower (8.0-8.1 km/s vs. ~8.2 km/s). This discrepancy might be due to the different frequency band of the two methods. The *SsPmp* observations we use has a center frequency of ~0.25 Hz, much lower than the active-source source data that has a dominant frequency of ~5 Hz (Fernández-Viejo et al., 2005). The lower frequency *SsPmp* samples a deeper part of the upper mantle than active-source *Pn*, suggesting V_p decreasing with depth, consistent with mineral-physics for typical lithosphere conditions (Garber et al., 2018). We caution that the uncertainty of the active-source *Pn* velocity (±0.1-0.2 km/s) (Fernández-Viejo et al., 2005) means this conclusion can only be tentative at this time.

T_{VDSS} is controlled by crustal thickness and V_p^{av} and can be measured together with Φ_{VDSS} by waveform fitting (Figs. 3 and 4). Whereas crustal thickness can be estimated from a single *SsPmp* observation with an assumed V_p^{av}, both H_{VDSS} and V_p^{av} can be constrained using multiple events recorded at the same station (Fig. 5; Kang et al., 2016). The uncertainties of our H_{VDSS} and V_p^{av} measurements (4.0 km and 0.20 km/s respectively) at YKW3 are larger than those given by Kang et al., 2016 for two stations in Australia (~3.0 km and ~0.15 km/s respectively). Three factors might contribute to the higher uncertainties of our measurements. First, the uncertainty of our T_{VDSS} (~0.3 s) is greater than Kang et al. (~0.18 s). Second, the ray parameter range of our

study (0.1247-0.1327 s/km) is smaller than both cases in Kang et al. (0.1223-0.1349 s/km for FORT and 0.1226-0.1369 s/km for WB2). Third, the number of events used in our study (7) is smaller than both cases in Kang et al. 2016 (20 for Fort and 12 for WB2). For the first factor, we note that whereas we compute T_{VDSS} uncertainties in a quantitative way (Supplementary Text 1), the uncertainties in Kang et al., 2016 are estimated empirically, making the T_{VDSS} uncertainties in the two papers not directly comparable. For the second and third factor, we note that we apply a very strict criterion for our data, so that the quality of Φ_{VDSS}, a less robust observable than T_{VDSS}, is guaranteed. Ideally, if only T_{VDSS} is concerned, we could lower our standard to include more events with wider p range, which might reduce the uncertainties of our estimated H_{VDSS} and V_p^{av} (Kang et al., 2016).

While inferring V_p^{um}, H_{VDSS} and V_p^{av} from Φ_{VDSS} and T_{VDSS} observations, we implicitly assume the CMB to be a sharp boundary as opposed to a broad transition zone. When the CMB is a velocity-gradient zone thinner than the dominant wave-length of the incident P wave (~25 km for typical field data), as we believe is true for most continental areas, Φ_{VDSS} is not significantly different from the case with a sharp CMB (Liu et al., 2018), thus our method of deriving V_p^{um} from Φ_{VDSS} still applies. When the CMB is a velocity-gradient zone with some of the $SsPmp$ rays turning in it ($1/p$ in the range of the gradient zone), the p-T_{VDSS} relation (moveout) is different from the case with a sharp CMB (Liu et al., 2018), making our method of deriving H and V_p^{av} from T_{VDSS} inaccurate. In such a case, if we know V_p^{um} either a priori or from Φ_{VDSS}, we could use only $SsPmp$ with turning velocities higher than V_p^{um} ($1/p > V_p^{um}$), so that all the reflections happen at the bottom of the CMB. In this way, we effectively measure the average V_p of the crust and the CMB.

The very good agreement between H_{VDSS} and H_{Hk} (Fig. 6) for the SW Slave Province not only demonstrates the robustness of our method, but also verifies the underlying assumptions that we make about the study area. First, the study area is well approximated with a 1D crustal model. Second, the CMB beneath the study area is likely a sharp boundary, so that $SsPmp$ reflections and Ps conversions happen at the same depth. Our PRF-VDSS joint analysis can constrain crustal average V_p/V_s ratio using only Ps conversions from PRFs. Our method is a significant development for two reasons. First, unlike conventional H-k stacking technique, our method does not require the presence of the Moho multiples ($PpPms$, $PpSms$ etc.), which are not always robustly observed. Second, in addition to k, our method also gives V_p^{av}, which is an input

parameter for conventional H-k stacking technique. Although a formal estimation of k_{Hk} uncertainty is not obtained here, based on the amplitude distribution of our H-k image, the uncertainty of k_{Hk} and k_{joint} are likely similar (Fig. 6). As mentioned above, if we include more events with a wider p range, the uncertainties of H and V_p^{av}, hence k_{joint}, are likely to further decrease.

When comparing our results with the Lithoprobe active-source results in the same area, we find that whereas the reflection Moho depth (~37.5 km; Hammer et al., 2010) agrees well with our results, the refraction Moho depth is significantly shallower (~34 km in Hammer et al., 2010 and ~31 km in Fernández-Viejo et al., 2005) than both our results and the reflection Moho (Fig. 9c). In addition, the crustal average V_p and V_p/V_s ratio derived from refraction experiments (~6.4 km/s and ~1.69 respectively; Fernández-Viejo et al., 2005) are both lower than our results (6.61±0.26 km/s and 1.747±0.08 respectively). Fernández-Viejo et al., 2005 interpreted their low crustal average V_p and V_p/V_s ratio as an evidence for a felsic composition of the crust in the SW Slave Province, whereas our results indicate an intermediate average crustal composition (Fig. 8). Fernández-Viejo et al. explained a reginal Bouguer gravity low with their silicic but thin crust; our intermediate but thicker crust is an equally consistent alternative. A trend of increasing crustal average V_p, V_p/V_s ratio and thickness with decreasing crustal age in the Western Australia Craton has been suggested to reflect a transition of crust-forming mechanism from plume tectonics to subduction-zone tectonics during Archean, which may also apply globally (Yuan, 2015). Within the framework of Yuan, 2015, our crustal average V_p, V_p/V_s ratio and thickness are most consistent with a Neoarchean age. We note that a more comprehensive study of crustal property and geological records in the Slave Province is needed to confirm if the model of Yuan 2015 is applicable to this area.

5. Conclusions

We show with synthetic and field examples that T_{VDSS} and Φ_{VDSS} can be used to estimate crustal average V_p, Moho depth and V_p of the uppermost mantle. We also demonstrate that we can acquire independent measurements of crustal average V_p/V_s ratio and composition with PRF-VDSS joint analysis. Our field example from the SW Slave Province show an intermediate crustal composition, which indicates a Neoarchean crustal age.

References:

Aki, K., Richards, P.G., 1980a. Phase shifts: phase delay and phase advance, in: Quantitative Seismology, Theory and Methods, Volume One. W. H. Freeman and Company, San Francisco, p. 156.

Aki, K., Richards, P.G., 1980b. Reflection and transmission of P-SV across a solid-solid interface, in: Quantitative Seismology, Theory and Methods, Volume One. W. H. Freeman and Company, San Francisco, pp. 144–151.

Bostock, M.G., 1998. Mantle stratigraphy and evolution of the Slave province. J. Geophys. Res. 103, 21183. doi:10.1029/98JB01069

Christensen, N.I., 1996. Poisson's ratio and crustal seismology. J. Geophys. Res. 101, 3139. doi:10.1029/95JB03446

Christensen, N.I., Mooney, W.D., 1995. Seismic velocity structure and composition of the continental crust: A global view. J. Geophys. Res. Solid Earth 100, 9761–9788. doi:10.1029/95JB00259

Cook, F.A., 2002. Fine structure of the continental reflection Moho. Bull. Geol. Soc. Am. 114, 64–79. doi:10.1130/0016-7606(2002)114<0064:FSOTCR>2.0.CO;2

Fernández-Viejo, G., Clowes, R.M., Welford, J.K., 2005. Constraints on the composition of the crust and uppermost mantle in northwestern Canada: Vp / Vs variations along Lithoprobe's SNorCLE transect. Can. J. Earth Sci. 42, 1205–1222. doi:10.1139/e05-028

Hammer, P.T.C., Clowes, R.M., Cook, F.A., van der Velden, A.J., Vasudevan, K., 2010. The Lithoprobe trans-continental lithospheric cross sections: imaging the internal structure of the North American continent. Can. J. Earth Sci. 47, 821–857. doi:10.1139/E10-036

Herrmann, R.B., 2013. Computer Programs in Seismology: An Evolving Tool for Instruction and Research. Seismol. Res. Lett. 84, 1081–1088. doi:10.1785/0220110096

Kang, D., Yu, C., Ning, J., Chen, W., 2016. Simultaneous Determination of Crustal Thickness

and *P* Wavespeed by Virtual Deep Seismic Sounding (VDSS). Seismol. Res. Lett. 87, 1104–1111. doi:10.1785/0220160056

Liu, T., Klemperer, S.L., Yu, C., Ning, J., 2018. Post-critical SsPmp and its applications to Virtual Deep Seismic Sounding (VDSS)—1: sensitivity to lithospheric 1-D and 2-D structure. Geophys. J. Int. 215, 880–894. doi:10.1093/gji/ggy307

Parker, E.H., Hawman, R.B., Fischer, K.M., Wagner, L.S., 2016. Estimating crustal thickness using SsPmp in regions covered by low-velocity sediments: Imaging the Moho beneath the Southeastern Suture of the Appalachian Margin Experiment (SESAME) array, SE Atlantic Coastal Plain. Geophys. Res. Lett. 43, 9627–9635. doi:10.1002/2016GL070103

Porritt, R.W., Miller, M.S., 2018. Updates to FuncLab, a Matlab based GUI for handling receiver functions. Comput. Geosci. 111, 260–271. doi:10.1016/j.cageo.2017.11.022

Randall, G.E., 1989. Efficient calculation of differential seismograms for lithospheric receiver functions. Geophys. J. Int. 99, 469–481. doi:10.1111/j.1365-246X.1989.tb02033.x

Snyder, D., Bruneton, M., 2007. Seismic anisotropy of the Slave craton, NW Canada, from joint interpretation of SKS and Rayleigh waves. Geophys. J. Int. 169, 170–188. doi:10.1111/j.1365-246X.2006.03287.x

Tian, X., Chen, Y., Tseng, T.L., Klemperer, S.L., Thybo, H., Liu, Z., Xu, T., Liang, X., Bai, Z., Zhang, X., Si, S., Sun, C., Lan, H., Wang, E., Teng, J., 2015. Weakly coupled lithospheric extension in southern Tibet. Earth Planet. Sci. Lett. 430, 171–177. doi:10.1016/j.epsl.2015.08.025

Tseng, T.L., Chen, W.P., Nowack, R.L., 2009. Northward thinning of Tibetan crust revealed by virtual seismic profiles. Geophys. Res. Lett. 36, 1–5. doi:10.1029/2009GL040457

Yu, C., Chen, W.P., van der Hilst, R.D., 2016. Constraints on residual topography and crustal properties in the western United States from virtual deep seismic sounding. J. Geophys. Res. Solid Earth 121, 5917–5930. doi:10.1002/2016JB013046

Yu, C.Q., Chen, W.P., Ning, J.Y., Tao, K., Tseng, T.L., Fang, X.D., John Chen, Y., van der Hilst, R.D., 2012. Thick crust beneath the Ordos plateau: Implications for instability of the North China craton. Earth Planet. Sci. Lett. 357–358, 366–375. doi:10.1016/j.epsl.2012.09.027

Yu, C.Q., Chen, W.P., Van Der Hilst, R.D., 2013. Removing source-side scattering for virtual deep seismic sounding (VDSS). Geophys. J. Int. 195, 1932–1941. doi:10.1093/gji/ggt359

Zhu, L., Kanamori, H., 2000. Moho depth variation in southern California from teleseismic

receiver functions. J. Geophys. Res. 105, 2969–2980. doi:Doi 10.1029/1999jb900322

(a)

V_p (km/s)

V_s (km/s)

ρ (g/cm³)

Depth (km)

CMB

(b)

Time (s)

Amplitude

$p = 0.127$ s/km

SsPmp

$A_{VDSS} = 0.86$

Ss

Sp

S
P

$\Phi_{VDSS} = 119°$
$T_{VDSS} = 6.95$ s

(c)

P wave   S wave

Receiver   Virtual
              source

Reflection
point

PRF

< 20 km

Crust

Mantle

Pp   *Ps*

VDSS

~ 60 km

Surface

CMB ≈ 40 km

SsPmp   *Ss*
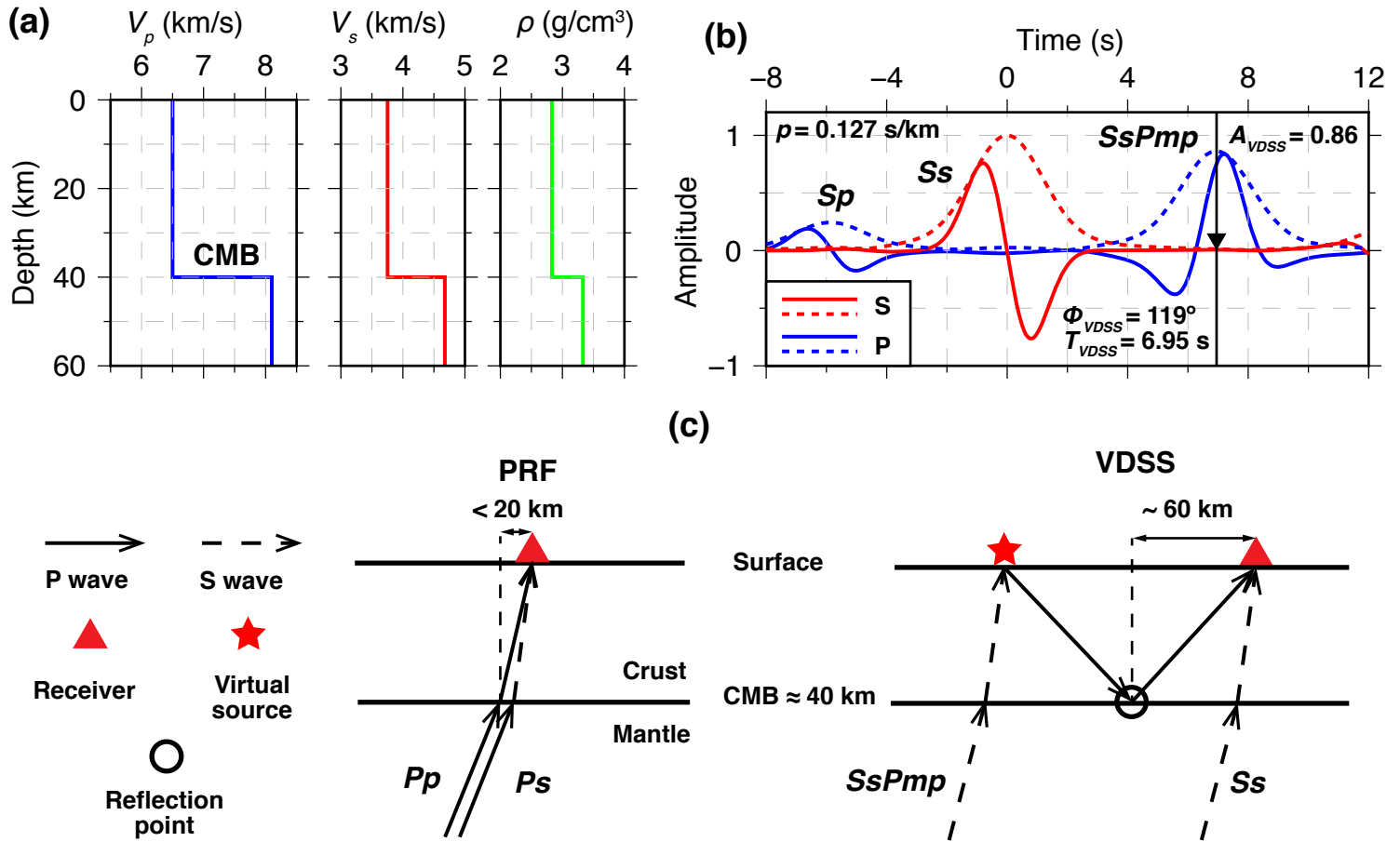
Figure 1. (a): 1D V_p, V_s and density model ('Model #1'). (b): P- and S-component synthetic seismograms ('observed waveforms') computed with Model #1for a ray parameter $p = 0.127$ s/km (epicentral distance of ~48.5º). The dashed curves are corresponding envelope functions. Here and throughout this paper, P-component is blue and S-component is red. Note the high amplitude and large phase shift of *SsPmp* relative to *Ss*. (c): Comparison between ray paths of P receiver functions (PRF) and Virtual Deep Seismic Sounding (VDSS).

(a)

(b)
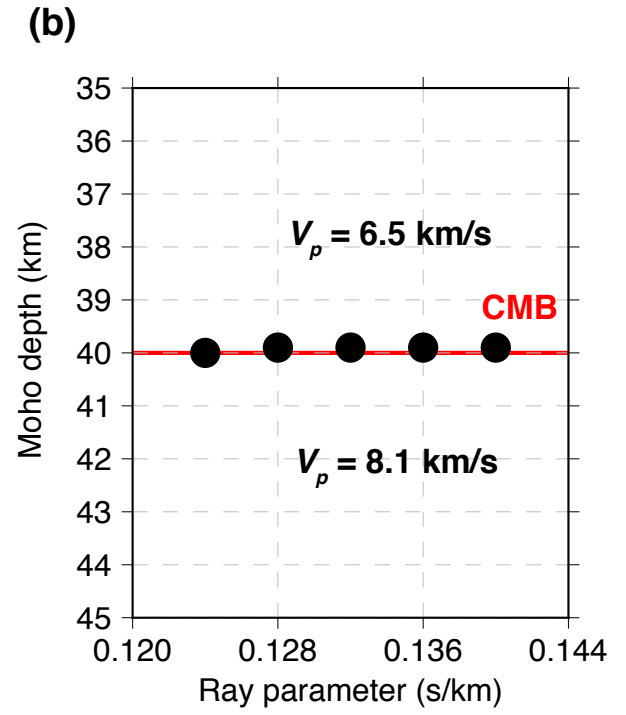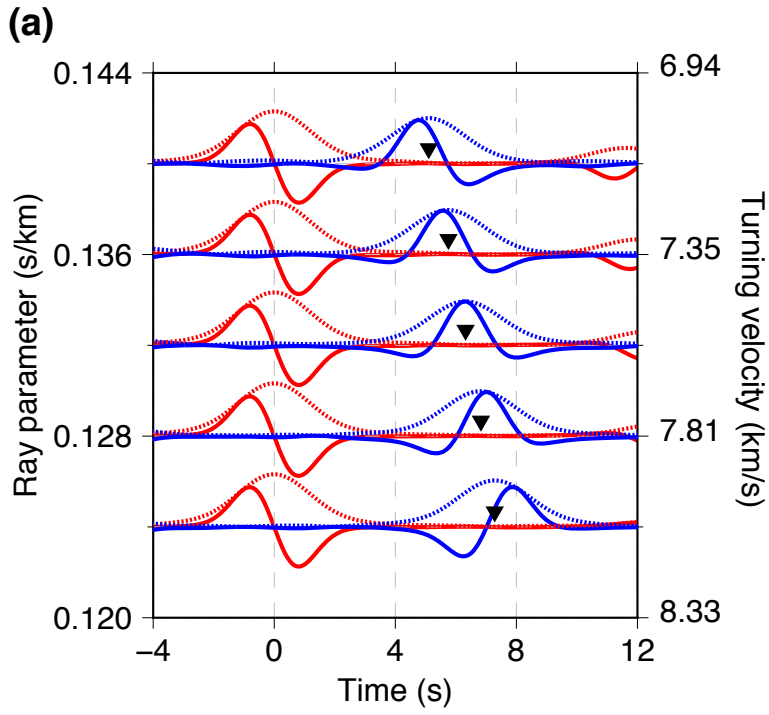
Figure 2. (a) Solid curves: P (blue) and S-component (red) synthetic waveforms ('observed waveforms') computed with Model #1 for ray parameter $p = 0.1240 – 0.1400$ s/km. Solid curves: blue is P- and red is S-component. Dotted curves: envelope functions. Black triangles: theoretical T_{VDSS} computed for Model #1, always located at the peak of the P-component envelope functions despite the change in Φ_{VDSS}. (b) Black circles: Moho depths derived from T_{VDSS} estimated by picking peaks on P envelope functions and converting to depth using the correct crustal average $V_p = 6.5$ km/s. Red line: true CMB depth at 40 km.

(a)

(b)

p = 0.128 s/km
1/p = 7.81 km/s

p = 0.136 s/km
1/p = 7.35 km/s

Upper-mantle V_p (V_p^{um}) (km/s)

Lower-crustal V_p (V_p^{lc}) (km/s)

Misfit

0.30
0.25
0.20
0.15
0.10
0.05
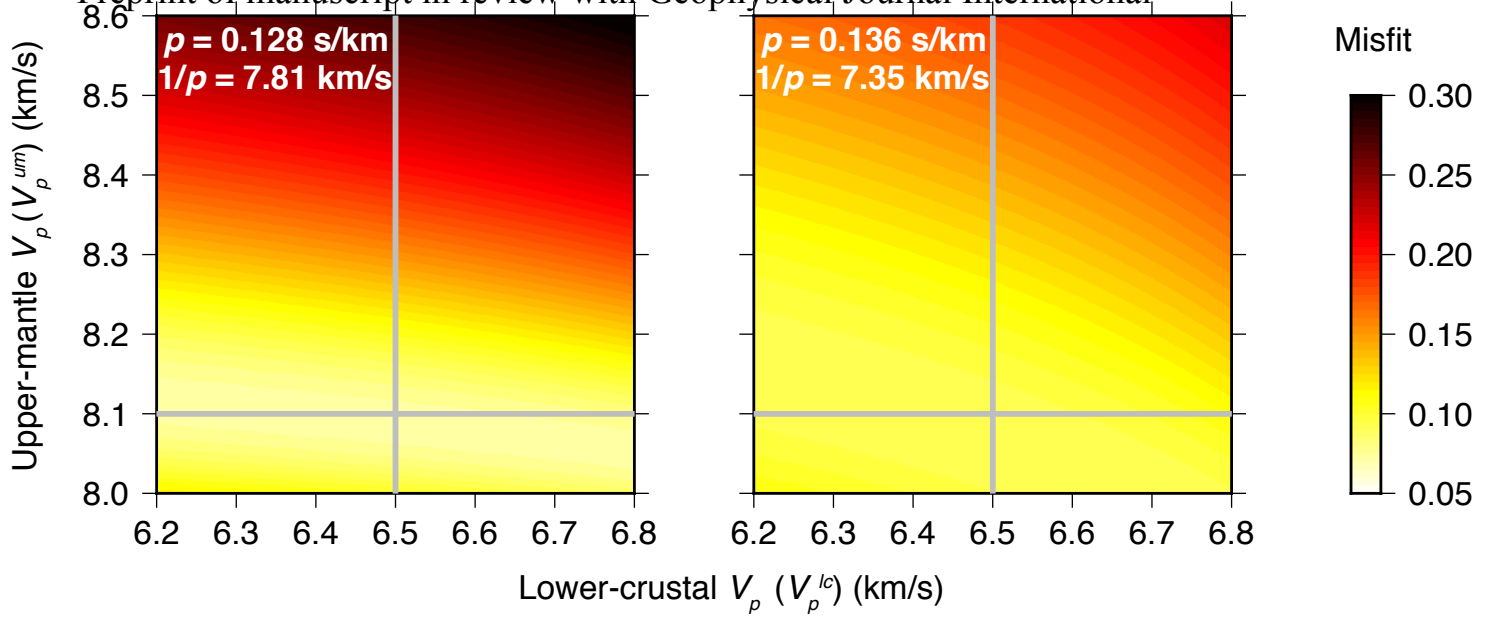
Figure 3. Normalized RMS misfit between synthetic waveforms generated with a grid search in $V_p^{um} - V_p^{lc}$ space and 'observed waveform' computed with Model #1 for (a) $p = 0.128$ s/km and (b) $p = 0.136$ s/km. Misfit is calculated over a 14-s wide window around $SsPmp$. Best fit to the 'observed waveform' is always at the Model #1 parameters (gray crosses), but V_p^{um} is most tightly constrained when the 'observed waveform' has $1/p$ close to the true V_p^{um} (from Model #1), i.e. far better for (a) $p = 0.128$ s/km (see Fig. 4d) than for (b) $p = 0.136$ s/km (see Fig. 4f).

Model #1
$p = 0.128$ s/km
$\Delta = 47.5°$

(a)

Depth (km)

$V_p^{lc} = 6.5$ km/s

$V_p^{um} = 8.1$ km/s

(b)

Amplitude

$p = 0.128$ km/s

Time (s)

Model #1
$p = 0.128$ s/km
$\Delta = 47.5°$

(c)

Depth (km)

$1/p = 7.81$ km/s

V_p^{lc} (km/s)
— 6.2
— 6.5
— 6.8

(d)

Normalized misfit

True V_p^{um}

V_p^{lc} (km/s)
— 6.2
— 6.5
— 6.8

Model #1
$p = 0.136$ s/km
$\Delta = 38°$

(e)

Depth (km)

$1/p = 7.35$ km/s

V_p (km/s)

(f)
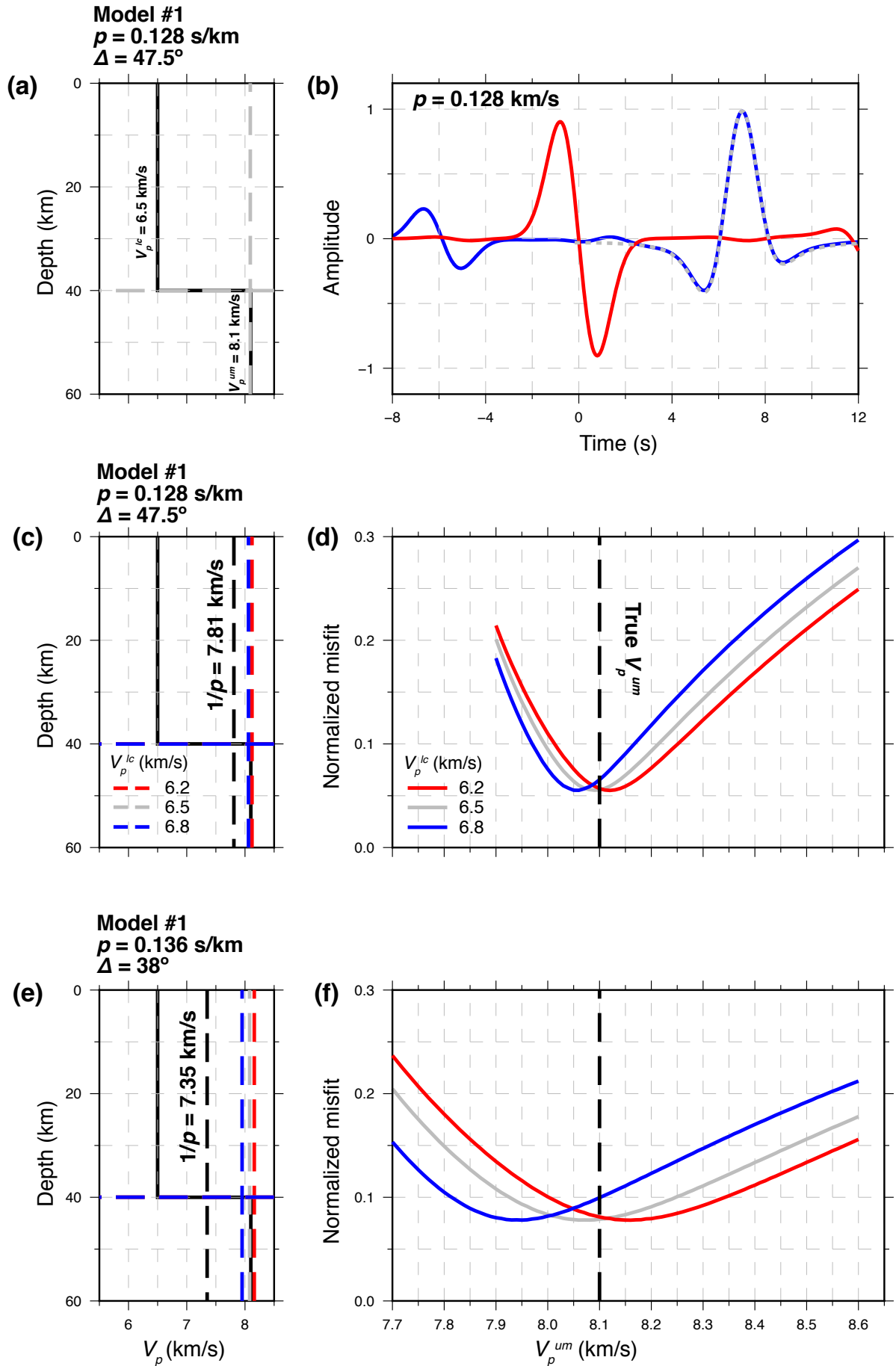
Normalized misfit

V_p^{um} (km/s)

Figure 4. Modelling Moho depth and V_p^{um} from waveforms computed for Model#1, with the additional constraint of an assumed V_p^{lc}. (a) and (b): modelling constrained using the correct $V_p^{lc} = 6.5$ km/s. (a): Gray dashed lines: Moho depth and V_p^{um} that best fit T_{VDSS} and Φ_{VDSS}, very closely matching Model #1 (black line). A crustal average $V_p^{av} = 6.5$ km/s is used to convert T_{VDSS} to Moho depth. (b): blue and red curves: synthetic P and S waveforms computed for Model #1 and $p = 0.128$ s/km ('observations'). Gray dashed curve: P-component $SsPmp$ waveform that best fits T_{VDSS} and Φ_{VDSS}. (c-f): A comparison of models using different assumed V_p^{lc}. (c) and (e): Model #1 as in (a) with Moho depths and V_p^{um} estimated for assumed $V_p^{lc} = 6.2$ (red), 6.5 (grey) and 6.6 (blue) km/s, for $p = 0.128$ and 0.136 s/km respectively. (d) and (f): Normalized misfits as functions of V_p^{um} for each case. Note the choice of V_p^{lc} has little effect on estimated V_p^{um} when p is small ($1/p$ is large and close to V_p^{um}; 4f), but has a significant effect when p is large ($1/p$ is small and far from V_p^{um}; 4g).
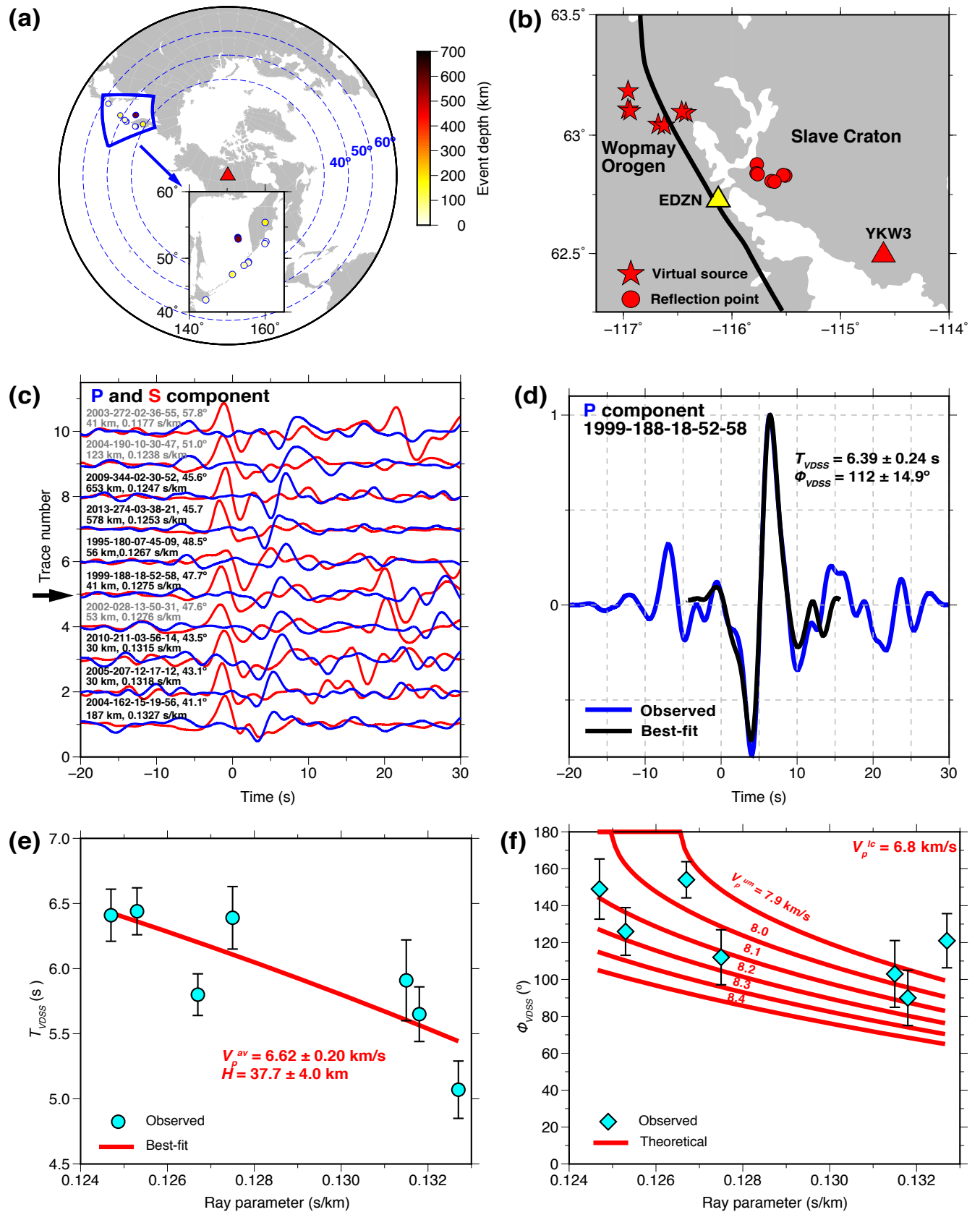
(a)

Event depth (km)

(b)

63.5°

63°

62.5°

Wopmay Orogen

Slave Craton

EDZN

YKW3

★ Virtual source

● Reflection point

−117° −116° −115° −114°

(c)

P and **S** component

2003-272-02-36-55, 57.8°
41 km, 0.1177 s/km

2004-190-10-30-47, 51.0°
123 km, 0.1238 s/km

2009-344-02-30-52, 45.6°
653 km, 0.1247 s/km

2013-274-03-38-21, 45.7
578 km, 0.1253 s/km

1995-180-07-45-09, 48.5°
56 km, 0.1267 s/km

1999-188-18-52-58, 47.7°
41 km, 0.1275 s/km

2002-028-13-50-31, 47.6°
53 km, 0.1276 s/km

2010-211-03-56-14, 43.5°
30 km, 0.1315 s/km

2005-207-12-17-12, 43.1°
30 km, 0.1318 s/km

2004-162-15-19-56, 41.1°
187 km, 0.1327 s/km

Trace number

Time (s)

(d)

P component
1999-188-18-52-58

$T_{VDSS} = 6.39 \pm 0.24$ s
$\Phi_{VDSS} = 112 \pm 14.9°$

— Observed
— Best-fit

Time (s)

(e)

T_{VDSS} (s)

$V_p^{av} = 6.62 \pm 0.20$ km/s
$H = 37.7 \pm 4.0$ km

● Observed
— Best-fit

Ray parameter (s/km)

(f)

Φ_{VDSS} (°)

$V_p^{lc} = 6.8$ km/s

$V_p^{um} = 7.9$ km/s

8.0
8.1
8.2
8.3
8.4

◆ Observed
— Theoretical

Ray parameter (s/km)

Figure 5. V_p^{um}, V_p^{av} and Moho depth H near station YKW3 derived from T_{VDSS} and Φ_{VDSS}. (a): Station YKW3 and ten earthquakes with back-azimuth 297–304°, Mw > 5.5, distance 40–60° and depth 30-700 km, colored by their focal depth. (b): Locations of stations (YKW3 and EDZN), Moho reflection points and virtual sources. The reflection-point and virtual-source locations are computed for the seven out of ten events in (a) with acceptable waveform misfits (see (c)) using the best-fit V_p^{av} and H (see (e)). The RF results of EDZN are shown in Fig. 7. (c): P and S component waveforms of the earthquakes used. The traces are sorted by their ray parameters (large to small) and labeled with their origin time, epicentral distance (in °), focal depth and ray parameter. Three traces with gray labels have high misfit and are not used in T_{VDSS} and Φ_{VDSS} analysis or shown in (b). Black arrow marks the event shown in (d). (d): Observed and best-fit P-component waveforms of Event 1999-188-18-52-58. (e): Observed T_{VDSS} as function of ray parameter (cyan circle), and best-fit relationship of V_p^{av} and H (red line) from linear regression (Kang et al., 2016.) (f): Observed Φ_{VDSS} as function of ray parameter (cyan diamond), and theoretical relations between Φ_{VDSS} and ray parameter for variable V_p^{um} (red curves) but V_p^{lc} fixed at 6.8 km/s. Observed Φ_{VDSS} favors V_p^{um} ~8.0–8.1 km/s.

(a) EDZN

$T_{Ps} = 4.24$ s

— Moveout-stacked RF

(b) % count

$T_{Ps} = 4.24$ s
$V_P^{av} = 6.62$ km/s

$k_{joint} = 1.745 \pm 0.061$

$H_{VDSS} = 37.7 \pm 4.0$ km

(c)

$H_{Hk} = 37.3$ km
$k_{Hk} = 1.754$

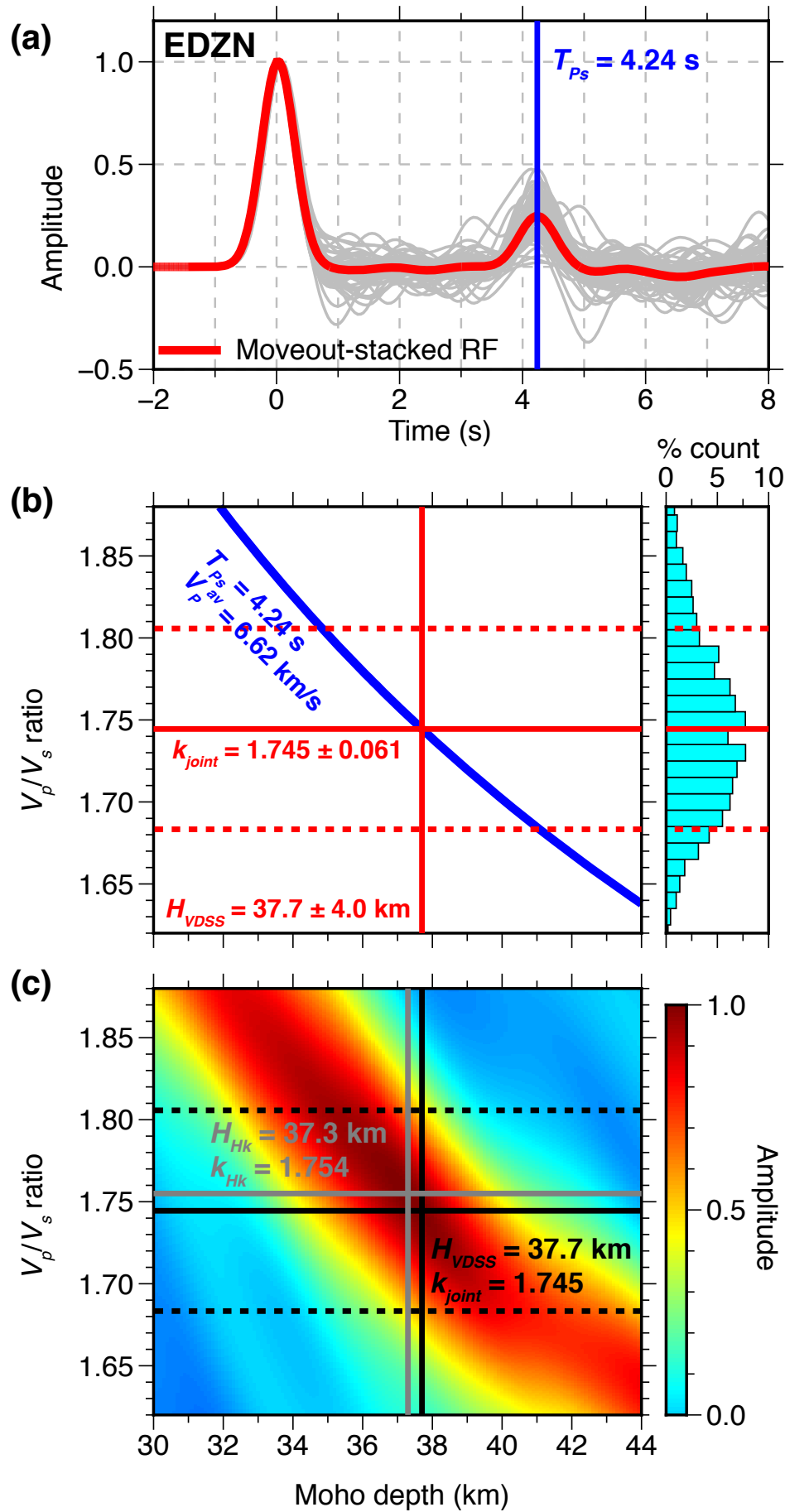$H_{VDSS} = 37.7$ km
$k_{joint} = 1.745$

Amplitude

Figure 6. PRF-VDSS joint analysis for crustal structure of SW Slave Province. (a): RF waveforms of EDZN. The stacked PRF is computed by summing 73 PRFs (gray curves) moveout-corrected to normal incidence. (b): Determination of crustal average V_p/V_s ratio (k_{joint}) from PRF T_{Ps} and VDSS Moho depth (H_{VDSS}) and crustal average V_p (V_p^{av}). The dashed gray lines mark the estimated uncertainty of k_{joint}, which is computed by taking the standard deviation of 5000 random simulations of k_{joint} (cyan histogram). (c): Comparison between H_{VDSS} and k_{joint} and H and k derived from conventional H-k stacking (H_{Hk} and k_{Hk}). Background color is normalized amplitude of the conventional H-k stack computed with $V_p^{av} = 6.62$ km/s and phase weight ratios $w_{Ps}:w_{PpPms}:w_{PpSms} = 1:0.5:0.5$. Note the close match between the two methods ($< 1\%$ difference).
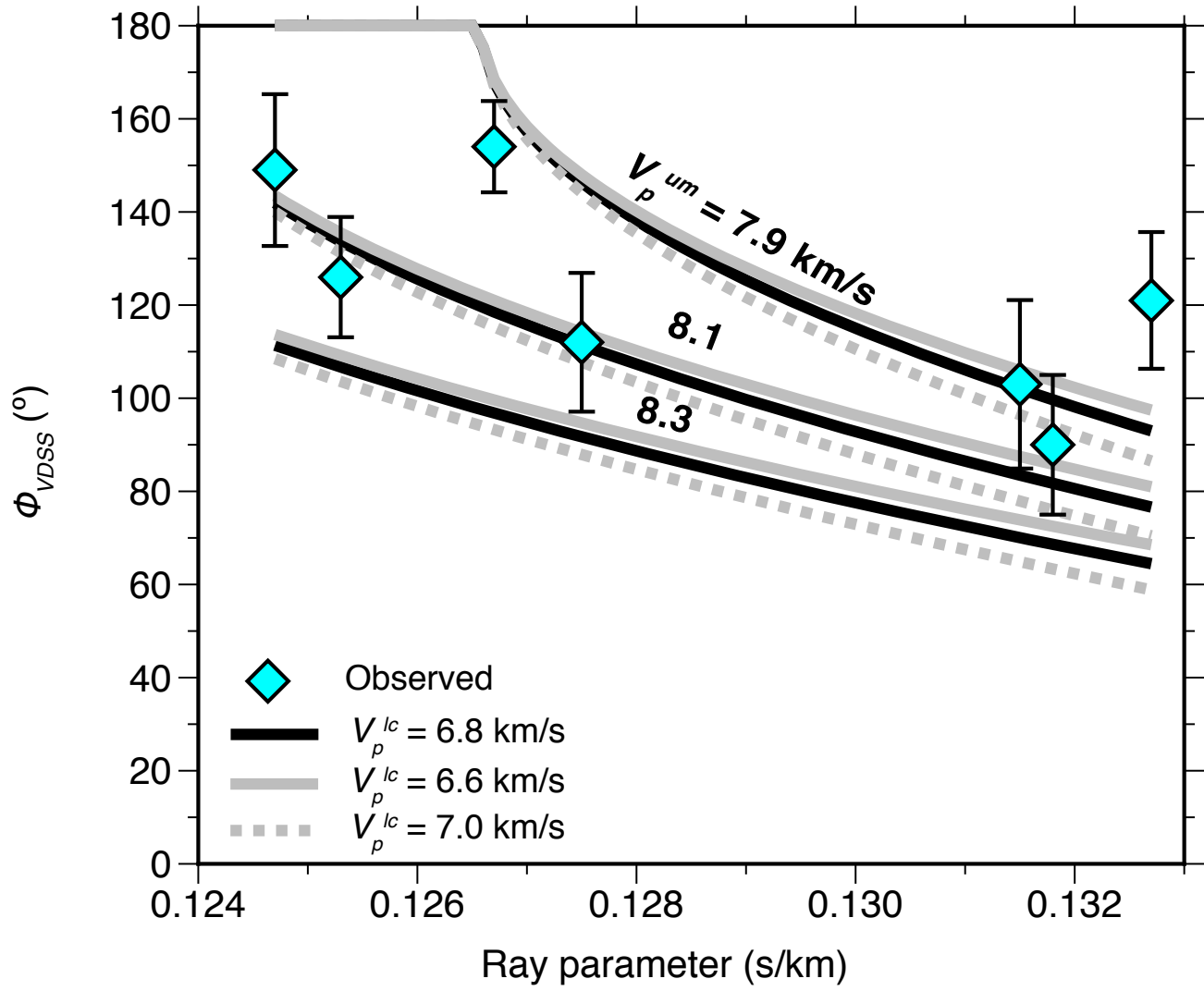
Figure 7. Effects of assumed V_p^{lc} on V_p^{um} derived from observed Φ_{VDSS} as a function of ray parameter. The black curves and data points are the same as the ones in Fig. 5(f).
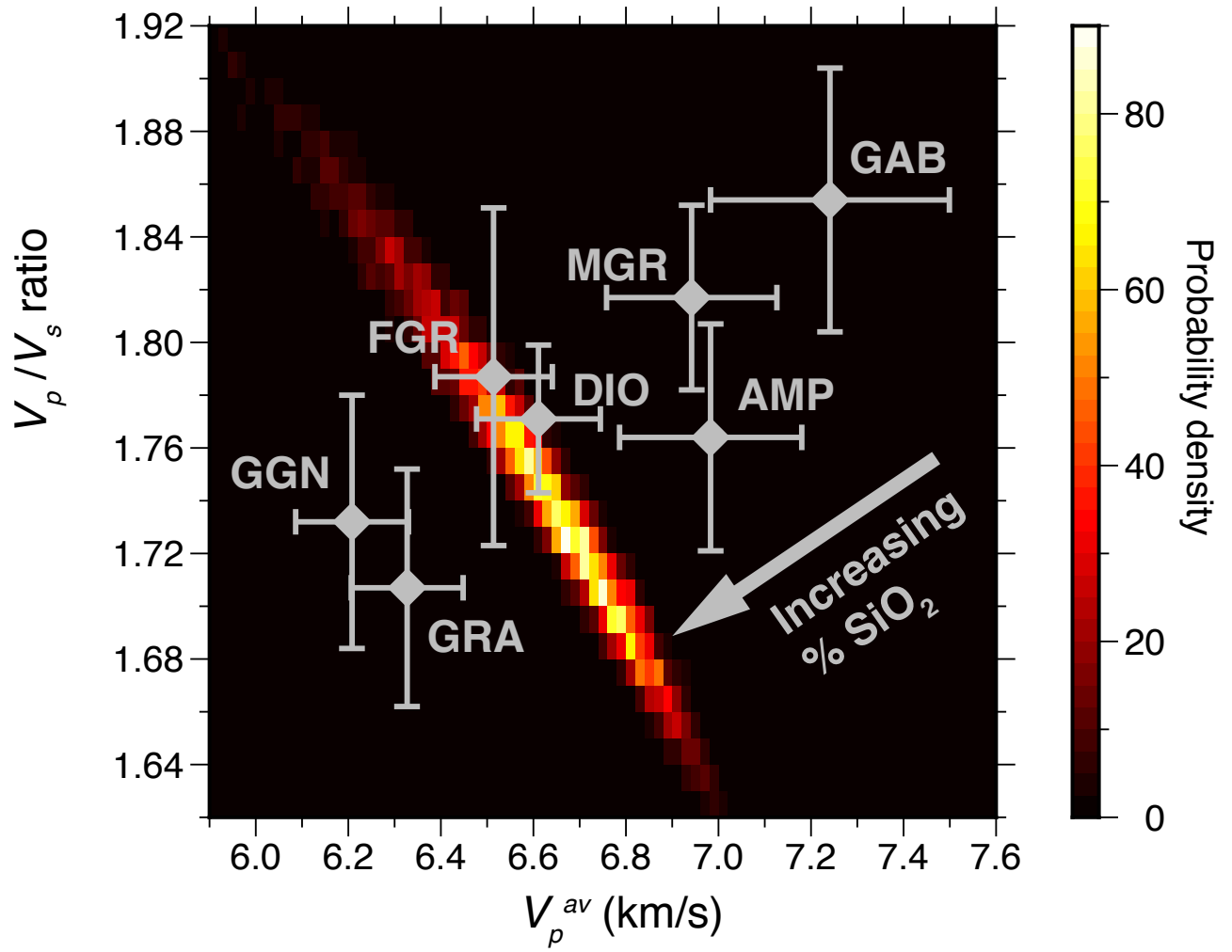
Figure 8. Constraining crustal average composition with RF-VDSS joint analysis. The probability density function is derived from 5000 random simulations of V_p^{av} and V_p/V_s ratio. The gray markers with error bars are measurements at 600 MPa and room temperature from Christensen 1996. GAB: Gabbro-norite-troctolite; MGR: Mafic granulite; DIO: Diorite; FGR: Felsic granulite; GGN: Granite gneiss; GRA: Granite-granodiorite; AMP: Amphibolite. Note a dioritic average composition matches our seismic observations best.

(a)

CORDILLERA — WOPMAY — SLAVE

64°

Deformed Ancestral North America

Anton

Rae-Edzo

Great Bear

Hottah

Yellowknife

Contwoyto

Fig. 5b

Fort Simpson

Great Slave Lake

Taltson

YK BC

NWT BC AB

Nahanni

8°

120°

km 300

WOPMAY / SLAVE

Great Bear / Anton / Contwoyto

(b)

S

Great Bear Magmatic Arc

N | W

Rae-Edzo

Yellowknife

Yellowknife Basin

E

Depth (km)

Hottah

Slave

Moho

8.2

8.2

Paleoproterozoic subduction

(c)

EDZN

YKW3

Depth (km)

Reflection Moho   Refraction Moho

Distance (km)

V_p (km/s)

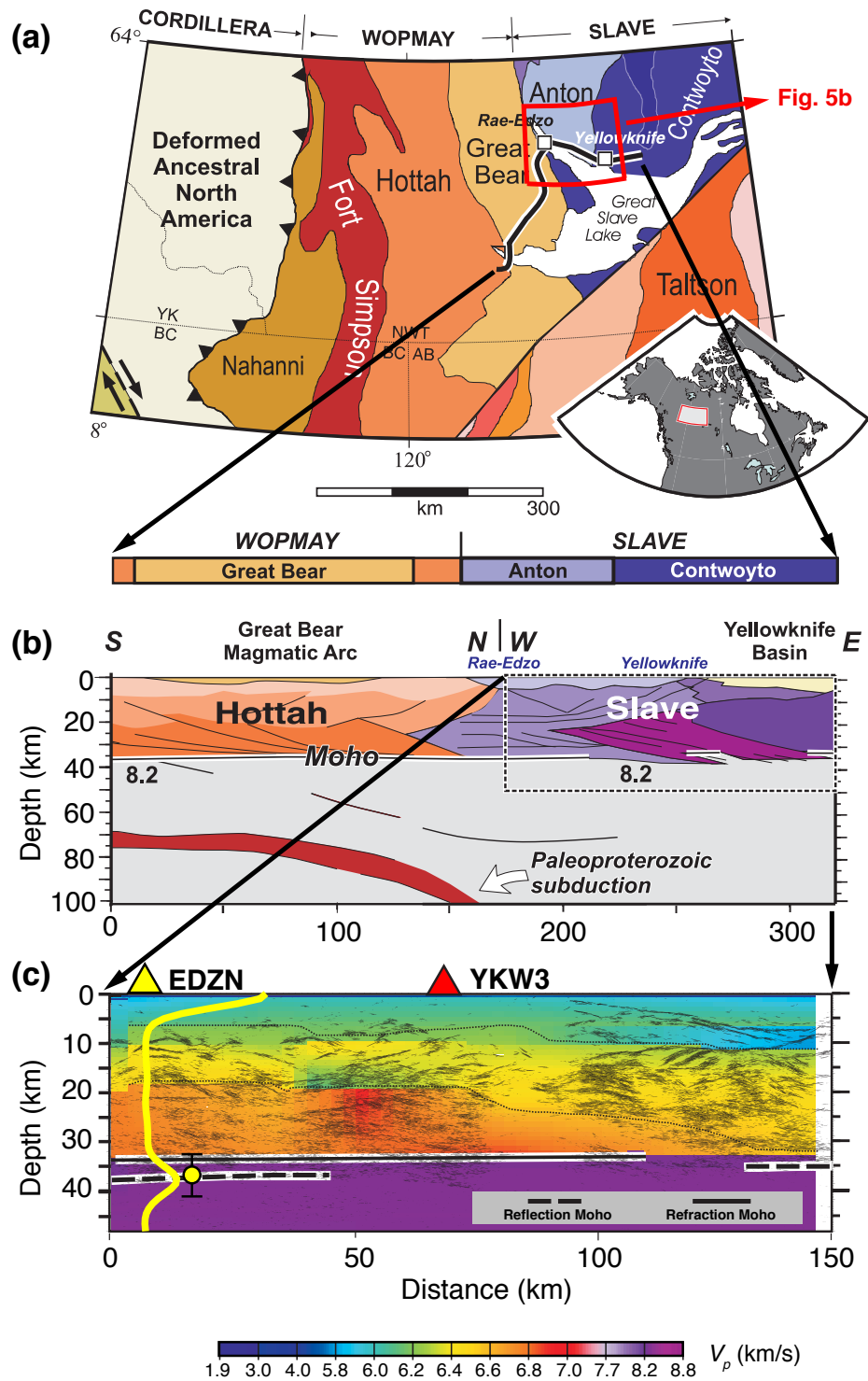1.9 3.0 4.0 5.8 6.0 6.2 6.4 6.6 6.8 7.0 7.7 8.2 8.8

Figure 9. Summary of VDSS, PRF, and the Lithoprobe active-source results in the SW Slave Province (reproduced from Hammer et al., 2010). (a): Map showing the Lithoprobe profiles Line 1 (solid line) on a simplified tectonic map of NW Canada. (b): Simplified interpretation based on the reflection and refraction results in (c). The bar at the top shows the geologic terranes along the profile. (c): Comparison between our VDSS and PRF and Lithoprobe reflection and refraction results. The migrated reflection image is overlain on the refraction V_p model. Yellow circle with error bars: VDSS Moho plotted at the reflection point. Yellow curve: moveout-stacked PRF mapped to depth domain and plotted at EDZN. Note that the VDSS, PRF and reflection Moho depths agree with each other (~37.5 km), whereas the refraction Moho (~34 km) is significantly shallower than them.